Prompt-neutron and prompt-gamma emission from a general description of the fission process (JEF/DOC 1423)[a]

Karl-Heinz Schmidt[b] and Beatriz Jurado[c]

Abstract: A semi-empirical model of the fission process is described, which covers most of the properties of the fission fragments and the emitted neutrons and photons in a global and consistent way. The model is based on fragment shells that are deduced from measured fission-fragment mass distributions, assuming that the macroscopic contribution of the compound nucleus and the microscopic contributions of the nascent fragments in the potential-energy surface are separable. The distributions of the collective coordinates are attributed to the motion of the quantum oscillators in their respective potential pockets perpendicular to the fission path. Different contributions to the excitation energies of the final fragments and their division at scission are described with the help of statistical mechanics. Intrinsic excitation energies of the fragments at scission are consistently described together with the even-odd effect in fission-fragment Z distributions. Mass-dependent equilibrium deformations of the nascent fragments are adjusted to measured average prompt-neutron multiplicities and attributed to fragment shells. A unique set of parameters is found, which reproduces a large variety of measured data for all fissioning systems with a good precision. In contrast to most available models, this approach is applicable to fissioning systems, for which no experimental data are available.

Introduction

Global parametrisations [1] and elaborate models [2, 3, 4] have been developed for calculating the energy spectra of prompt fission neutrons and their multiplicity distributions. Most of them are based on measured mass-TKE distributions of the fission fragments. With the help of the Q values for specific nuclear-charge and mass splits and by considering the initial excitation energy, the total excitation energy TXE of the fragments can directly be deduced. With an assumption on the division of the TXE between the fragments, which needs to be consistent with the observed mass-dependent neutron multiplicities, the initial conditions of both fragments for a statistical de-excitation code of the Weisskopf or Hauser-Feshbach type are determined.

The task is appreciably more difficult when this experimental basis, the measured mass-TKE distribution, is not available. In this case, this information may be provided by a model calculation. The GEF code has been developed for this purpose. It is a semi-empirical model of the fission process, which covers most of the properties of the fission fragments and the emitted neutrons and photons in a global and consistent way. In addition to the mass-TKE distribution it also calculates the division of the TXE between the fragments and the angular momenta of the fragments. Moreover, the specific initial conditions of each individual fragment are given. This report gives an overview on the underlying physics ideas and the technical features of the code and presents some results.

Fission channels

Experimental systematics

Figure 1 gives an overview of measured mass and nuclear-charge distributions of fission products from low-energy fission. Fission of target nuclei in the actinide region, mostly induced by neutrons, shows predominantly asymmetric mass splits. A transition to symmetric mass splits is seen around mass 258 in spontaneous fission of fusion residues. Electromagnetic-induced fission of relativistic secondary beams covers the transition from asymmetric to symmetric fission around mass 226 [5]. A pronounced fine structure close to symmetry appears in ^{201}Tl [6] and in ^{180}Hg [7]. It is difficult to observe low-energy fission in this mass range. Thus, ^{201}Tl could only be measured down to 7.3 MeV above the fission barrier due to its low fissility, which explains the filling of the minimum between

a This report has been produced in the frame of a consultant contract of K.-H. S. with the NEA of OECD.

b E-mail: schmidt-erzhausen@t-online.de, URL: http://www.khs-erzhausen.de

c E-mail: jurado@cenbg.in2p3.fr, CENBG, CNRS/IN2 P3, Chemin du Solarium B.P. 120, F-33175 Gradignan, France

the two peaks. Only ^{180}Hg was measured at energies close to the barrier after beta decay of ^{180}Tl. Considering the measured energy dependence of the structure for ^{201}Tl [6], the fission characteristics of these two nuclei are rather similar. Also other nuclei in this mass region show similar features, which have been attributed to the influence of fragment shells [8]. It is interesting to note that the shell at N=68 postulated in ref. [8] nearly coincides with the shell at Z=44 that modulates the S1 channel in the GEF code (see Appendix 1) in the fragments measured in ref. [6].

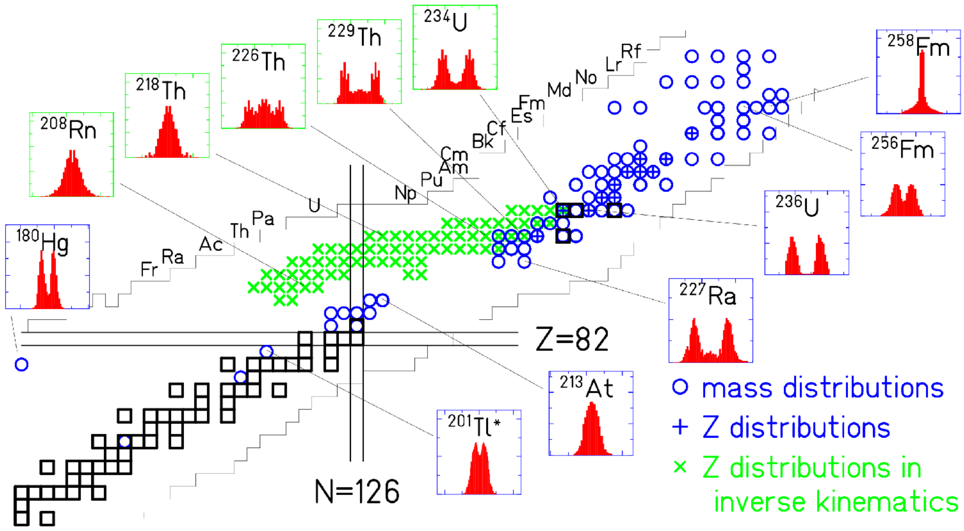

Figure 1. *General view on the systems for which mass or nuclear-charge distributions have been measured. The distributions are shown for 12 selected systems. Blue circles (blue crosses): Mass (nuclear-charge) distributions, measured in conventional experiments [6, 7], and references given in [5]. Green crosses: Nuclear-charge distributions, measured in inverse kinematics [5].*

Size of the heavy fragment in asymmetric fission

In the range where asymmetric fission prevails, e.g. from ^{227}Ra to ^{256}Fm, the light and the heavy fission-product components gradually approach each other, see figure 1. A quantitative analysis reveals that the mean mass of the heavy component stays approximately constant [9] at about A=140. This has been explained by the influence of a deformed (β≈0.6) fragment shell at N=88 and the spherical shell at N=82 [10], suggesting that the position of the heavy fragment is essentially constant in neutron number.

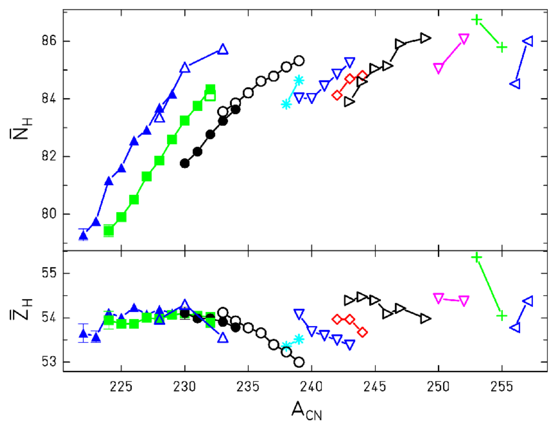

Figure 2. *Mean neutron and proton number of the heavy component in asymmetric fission in the actinide region. The values were deduced from measured mass and nuclear-charge distributions using the semi-empirical GEF code [11] for the correction of charge polarization and prompt-neutron emission. Open symbols denote results from conventional experiments, full symbols refer to an experiment with relativistic projectile fragments of ^{238}U [5]. Data points for the same Z_{CN} are connected. (See [11] for references of the underlying experimental data.)*

New data on Z distributions over long isotopic chains [5], however, reveal very clearly that the position in neutron number varies systematically over more than 7 units, while the position in proton number is approximately constant at Z=54, see figure 2. The rather short isotopic sequences covered in former experiments did not show this feature clearly enough and gave the false impression of a constant position in mass.

This finding represents a severe puzzle to theory, since shell-model calculations do not show any shell stabilization near Z=54 at $\beta\approx0.6$ [10,[12]].

Separability principle

The microscopic-macroscopic approach has proven to be very useful for calculating nuclear properties, in particular in applications to fission [[13]]. The early influence of fragment shells on the fission path, deduced from two-centre shell-model calculations [[14]], makes its application to fission even more powerful. It means that the microscopic properties of the fissionning system are essentially determined by the shells of the *fragments*, and only the macroscopic properties are specific to the *fissioning system* [[15]].

This "separability principle" was exploited in the GEF code [11], which relies on an empirical description of the macroscopic stiffness parameters in the relevant normal modes [[16]] (excitations perpendicular to the fission path) and empirically deduced fragment shells, which are valid for all fissioning systems. Figure 3 demonstrates that the mass distributions over a large range of systems can be described very well with the same parameter set. A comprehensive overview on many mass distributions is given in Appendix 2.

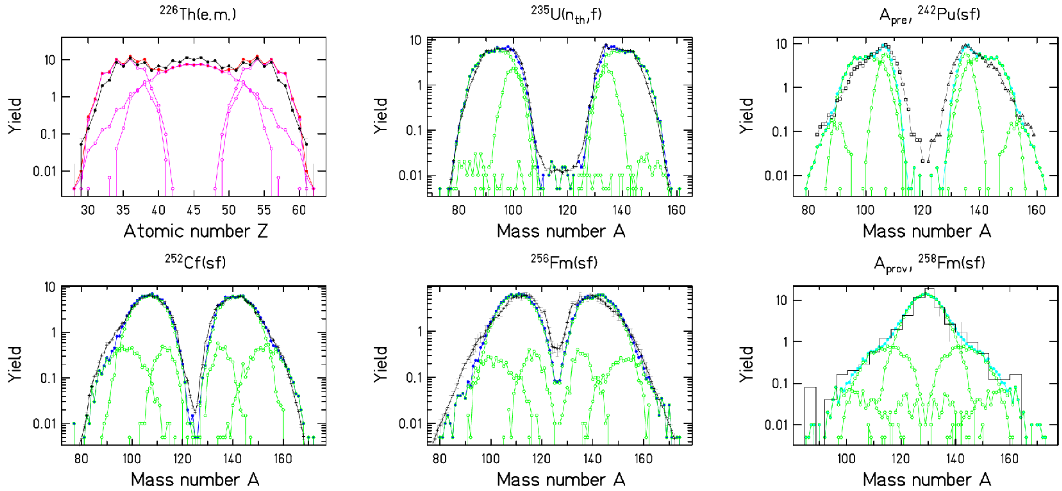

Figure 3. *Nuclear-charge and post-neutron mass distributions of fission fragments. (For ^{258}Fm(sf) the "provisional mass" A_{prov} is shown, which is directly deduced from the ratio of the kinetic energies of the fragments and thus not corrected for neutron emission.) Experimental data (black lines, respectively histogram) for electromagnetic-induced (e.m.), thermal-neutron-induced (n_{th},f) and spontaneous fission (sf) are compared with predictions of the GEF code [11] (red and green lines). The contributions of different fission channels are shown. (See [11] for references of the data.)*

Dynamical effects

Statistical scission-point models, e.g. ref. [10], suffer from the neglect of dynamical effects. Stochastic calculations revealed that, depending on the nature of the collective degree of freedom, dynamical effects induce a kind of memory on the fission trajectory, which may be accounted for by an early freeze-out that depends on the influence of inertia. Mass-asymmetric distortions have a large inertia, and thus the mass distribution is already essentially determined slightly behind the outer fission saddle [[17]]. Charge polarization has a small inertia, and the distribution is determined close to scission [[18]]. Other quantities that change during the descent from saddle to scission, e.g. the intrinsic excitation energy, have less effect on the fission observables, since the normal modes are hardly excited, see next section.

Quantum-mechanical effects

Most fission observables form bell-shaped distributions around a mean value. This suggests treating the corresponding collective degree of freedom as an harmonic quantum oscillator coupled to a heat bath of temperature *T*. Especially for the charge-polarization degree of freedom there is a long discussion about the importance of the zero-point motion [[19], [20]]. Nix estimated the level spacing in the oscillator corresponding to mass-asymmetric distortions at saddle with the liquid-drop model to 1-2 MeV in the actinide region [16]. According to the smaller widths of the corresponding components to the mass distribution, the level spacing for oscillations in the two asymmetric fission valleys (Standard 2 and Standard 1) is about 5 and more than 10 MeV, respectively. Also for oscillations in the charge-polarization degree of freedom, the level spacing is in the order of 10 MeV. These values are appreciably larger than the temperature values of actinides, which are about 0.5 MeV in the constant-temperature regime [[21]]. Thus, in a statistical approach these degrees of freedom are essentially not excited, and the widths of the corresponding distributions are essentially determined by the zero-point motion.

Also the angular-momentum distributions of the fragments have been explained by "orientation pumping" due to the uncertainty principle [[22]]. Experimental indications for thermal excitations of spherical fragments [[23]] have also been explained by the compensation of the orbital angular momentum, which itself is induced by the zero-point motion [[24]]. Here it is the operator of the orbital angular momentum which does not commute with the angle that characterizes the direction of particle motion. Thus, all fragment angular momenta measured in low-energy fission [[25]] are explained by the quantum-mechanical uncertainty principle. There is no room for excitations of the angular-momentum-bearing modes [[26]].

Due to the strong influence of quantum-mechanical effects it is mandatory to explicitly consider these quantum-mechanical effects, as it is e.g. done in the self-consistent microscopic approach of ref. [[27]]. Stochastic approaches with classical models [[28]] seem to be inadequate.

Comparison with previous ideas

Several descriptions of the fission observables with applications of the statistical model have been proposed in the past. The present approach is rather close to the outline of a scenario proposed by Jensen and Døssing [[29]], although the present model covers a larger variety of observables. More importantly, it also tries to better exploit available empirical information.

Jensen and Døssing presented a statistical calculation of the mass distribution in fission with some ideas about the dynamics of the process. The most important modifications applied in the GEF code are: (i) The shell effects that were calculated from single-particle energy spectra in a Woods-Saxon potential with the Strutinsky method in ref. [[29]] are replaced by global fragment shells, which are adjusted to the measured mass distributions. The separability principle simplifies this task considerably, since the fragment shells are assumed to depend only on the fragment, and, thus, they are the same for all fissioning systems. (ii) The nuclear level density that was calculated from the same single-particle spectrum including pairing correlations using the BCS approximation in ref. [[29]] is replaced by an empirical constant-temperature formula [21], which seems to be in good agreement with recent experimental results [[30]]. (iii) The influence of quantum-mechanics, in particular the zero-point motion, has been considered to model the distributions of collective coordinates. They are attributed to the motion of the quantum oscillators in their respective potential pockets perpendicular to the fission path. The parameters of these oscillators are deduced from experimental data. In addition, the shapes of the fragments at scission, the charge polarization, the angular momenta, and other properties of the fragments are calculated on the basis of similar ideas.

Prompt-neutron yields

Transformation of energy – the different contributions

In low-energy fission, the Q value of the reaction ends up either in the total kinetic energy (TKE) or the total excitation energy (TXE) of the fragments. The TKE is closely related to the distance of the

centres of the two nascent fragments at scission, but it cannot give information on the shapes of the individual fragments. The TXE, however, can be attributed to the individual fragments by a kinematical measurement of the prompt-neutrons, since the total energy emitted by prompt gamma radiation can be estimated from systematics rather well. Still, there is no direct experimental information on the processes, which are responsible for the transformation of part of the Q value into the excitation energies of the separated fragments. The situation is schematically illustrated in figure 4. Before scission, dissipation leads to intrinsic excitations, collective modes perpendicular to the fission direction ("normal modes" [16]) may be excited, and, finally, some energy is stored in deformation of the nascent fragments that is induced by the Coulomb repulsion. The remaining part is found as pre-scission kinetic energy [31]. After scission, collective excitations and deformation energy are transformed and add up to the intrinsic excitations of the separated fragments.
The situation at scission is important for the understanding of fission dynamics, e.g. the magnitude of dissipation and the coupling between the different collective degrees of freedom, but without additional information, the repartition of the different contributions between the fragments remains ambiguous.

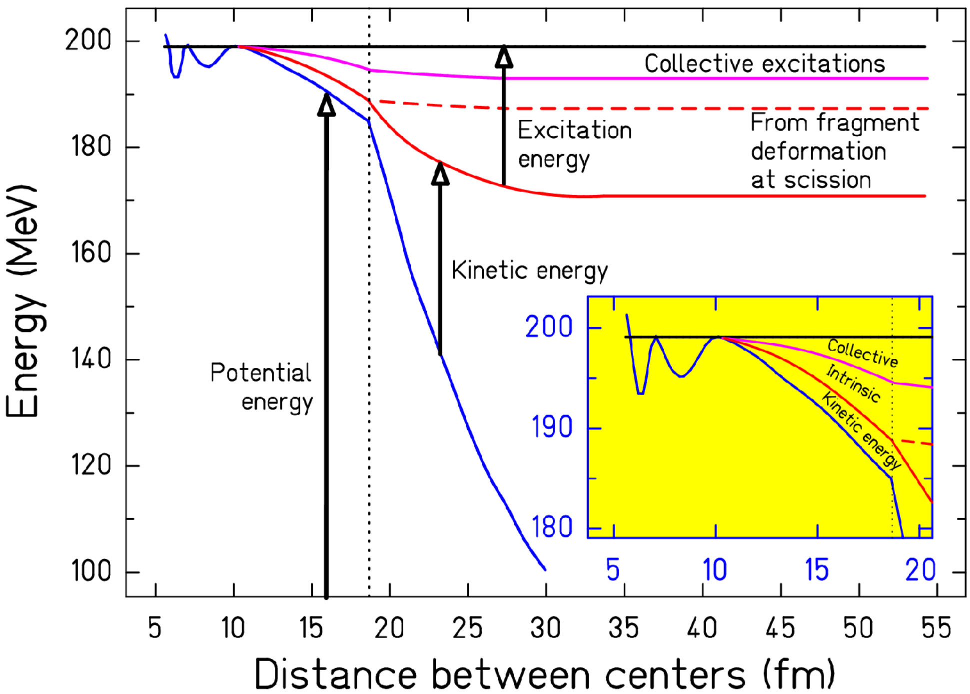

Figure 4. *Schematic drawing of the transformation of energy during the fission process of ^{236}U with an initial excitation energy equal to the height of the fission barrier. The vertical dotted line indicates the scission point, and the inset represents a zoom of the situation at scission. (Adapted from figs. 7 to 9 of ref. [32].)*

Origin of the saw-tooth shape

There is widespread agreement that the saw-tooth shape of the prompt-neutron yields, see figures 5 and 6, is caused by the deformation energies of the nascent fragments at scission. The scission-point model of ref. [10] attributes it to the influence of fragment shells, the random-neck-rupture model [33] links it to the location of the rupture, and also microscopic calculations predict large deformation energies of the fragments near scission [34]. Large even-odd effects in the fragment Z distributions indicate that the intrinsic excitation energy at scission is generally much too low to account for the variation of the prompt-neutron yield by several units over the different fragments.
The GEF calculations, shown in addition, were performed with the assumption that the deformation of the nascent fragments is given by the same function of the fragment proton number for all

systems (see Appendix 1), requiring that the well-known total neutron multiplicities are well reproduced (table 1).

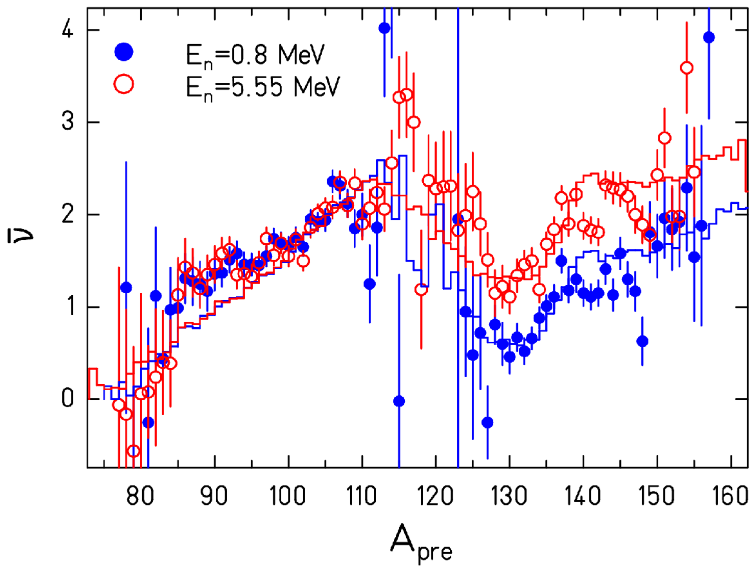

Figure 5. *Measured mean prompt-neutron yield in ^{237}Np(n,f) as a function of pre-neutron mass at two different incident-neutron energies [35] (data points) in comparison with the result of the GEF code [11] (histograms).*

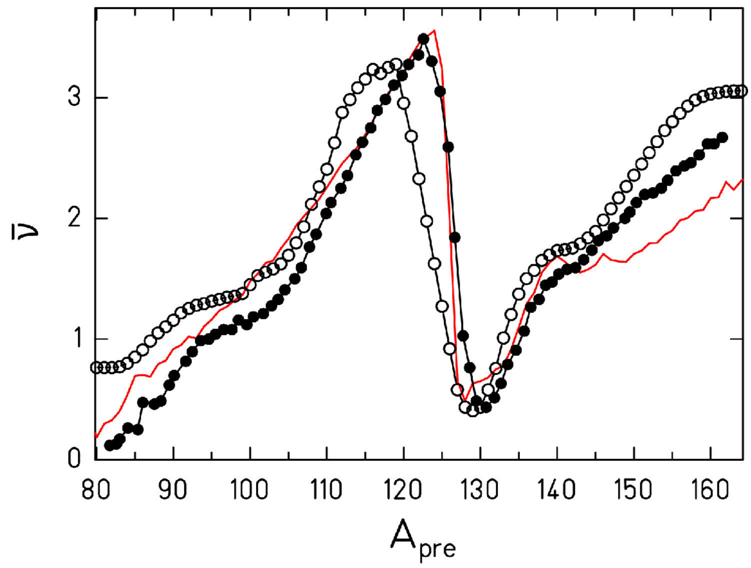

Figure 6. *Measured mean prompt-neutron yield in ^{252}Cf(sf) as a function of pre-neutron mass from ref. [36] (full symbols) in comparison with the result of the GEF code [11] (red line). Error bars given in ref. [36] are smaller than the symbols. The systematics of Wahl [37] (open symbols) based on 5 older experiments that is shown in addition gives an idea about the magnitude of the discrepancies between different experiments.*

Energy dependence of the neutron yields – energy sorting

Recent experimental results reveal that nuclei exhibit an essentially constant temperature, may be up to excitation energies of 20 MeV [38] with a temperature parameter that is grossly proportional to $A^{-2/3}$ [21]. This behaviour is explained by the breaking of pairs in the so-called superfluid regime [39]. This leads to a considerable increase of the heat capacity [40] and consequently to a slow variation of temperature as a function of excitation energy. Thus, the assumption of a constant

nuclear temperature becomes a good approximation. This implies that the intrinsic excitation energy of the two nascent fragments at scission is subject to energy sorting [41, 42, 43]: The hotter light fragment transfers almost all its intrinsic excitation energy to the colder heavy fragment. This energy sorting manifests itself in the mass-dependent neutron yields. Fig. 5 shows data for neutron-induced fission of ^{237}Np with E_n = 0.8 MeV and E_n = 5.55 MeV as an example. The additional initial energy leads to an increased neutron yield from the heavy fragments, only. The behaviour is well reproduced by the GEF code, which includes a model for the process of energy sorting.
Note that the BCS approximation severely underestimates the pairing condensation energy and consequently also the magnitude of the heat capacity in the so-called superfluid regime [44]. Thus, the constant-temperature description might be approximately valid up to higher energies than usually considered, e.g. in ref [45].

Even-odd effect in Z yields

Experimental systematics

A systematic view on the local even-odd effect in fission-fragment *Z* distributions [46] reveals a regular pattern and a general dependence on the fissioning system, see figure 7. The magnitude of the even-odd effect is small at symmetry, and it increases strongly with increasing asymmetry. At the same time, the even-odd effect generally decreases for heavier systems. The even-odd effect in the light fragment group of nearby even-*Z* and odd-*Z* systems is essentially identical, except at symmetry, where the even-odd effect in odd-*Z* systems is exactly zero. Electromagnetic excitations lead to slightly higher excitation energies, thus reducing the magnitude of the even-odd effect. The large number of systems investigated revealed that the appearance of a large even-odd effect at large asymmetry is a general phenomenon, also in odd-Z fissioning systems [47]. In any case, there is an enhancement of even-Z fragments in the light fragment group, indicating that it is the enhanced production of even-Z light fragments in their "ground state" at scission, which is at the origin of the large even-odd effect at extreme asymmetry.

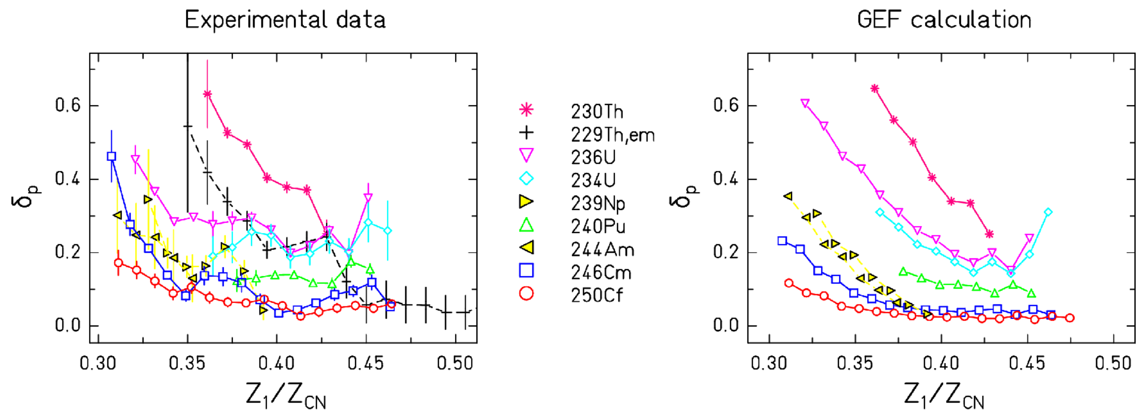

Figure 7. *Measured (left) and calculated (right) local even-odd effect in fission-fragment Z distributions in (n_{th},f) reactions. The fissioning nuclei are indicated. Data for fission of ^{229}Th, induced by electromagnetic excitations are included. See ref. [46] for references of the data.*

Final stage of energy sorting

It seems straightforward to attribute the enhanced production of even-*Z* light fragments to the energy-sorting mechanism [48] that explained already the differential behaviour of the prompt-neutron yields. If the time until scission is sufficient for the energy sorting to be accomplished, the system can still gain an additional amount of entropy by predominantly producing even-even light fragments. Compared to the production of odd-odd light fragments, the excitation energy of the heavy fragment increases by two times the pairing gap, and its entropy increases due to the increasing number of available states in the heavy fragment. The right part of figure 7 shows a calculation with the GEF code, where this idea is included in a schematic way. The basic features

are: (i) The excitation energy induced by dissipation grows with the Coulomb parameter $Z^2/A^{1/3}$, and the time needed for complete energy sorting is correspondingly increased. This explains the observed reduction of the even-odd effect for heavier systems. (ii) The thermal pressure between the two nascent fragments grows with increasing asymmetry, which accelerates the energy-sorting process. This explains the strong increase of the even-odd effect at large asymmetry.
The asymmetry-driven even-odd effect is thus a threshold phenomena, which sets in when the time needed for reaching the scission configuration is sufficiently long for complete energy sorting. Fluctuations in the energy-sorting process are responsible for the smooth onset of the even-odd effect with increasing asymmetry.

Charge polarization

The fission fragments are not fully specified by their mass number. While the total numbers of protons and neutrons of the two fission fragments at scission, i.e. before prompt-neutron emission, are given by the fissioning nucleus, the *N/Z* ratios of the fragments may be different. One fragment may be more, the other one less neutron-rich. This “charge polarization“ is essentially characterized by its mean value and its width.

Experimental information
Most experimental information on charge polarization at scission is indirect, because only the fragment masses after the emission of prompt neutrons can be measured with good resolution. Thus, the influence of prompt-neutron emission has to be corrected. This correction introduces some uncertainties, because most data on mass-dependent prompt-neutron multiplicities are not very precise, and for many systems such data are not available.
Figure 8 shows the measured deviation of the mean nuclear charge from the UCD (unchanged charge distribution) value for a fixed post-neutron mass and the standard deviation of the corresponding nuclear-charge distribution for the thermal-neutron-induced fission of ^{235}U [49]. The influence of the even-odd staggering of the *Z* yields is clearly visible in both quantities.

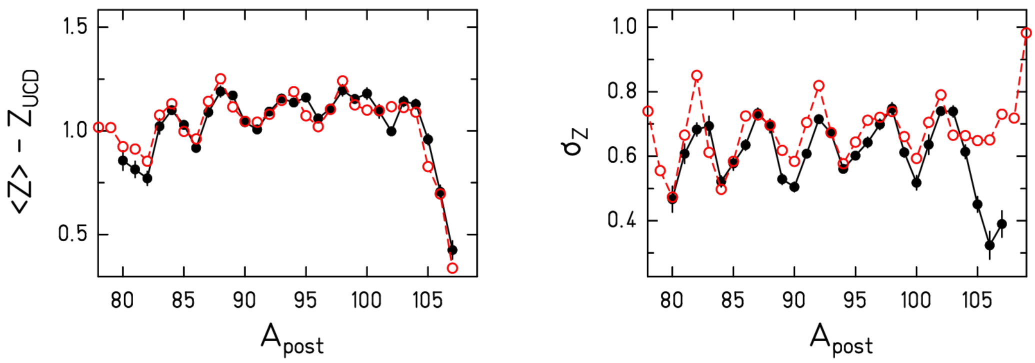

Figure 8. *Indirect information on the charge polarization in $^{235}U(n_{th},f)$. Left part:Deviation of the mean nuclear charge from the UCD (unchanged charge distribution) value for a fixed post-neutron mass A_{post}. Experimental data [49] (full points) are compared with the result of the GEF code [11] (open points). Right part: Standard deviation of the nuclear-charge distribution for a fixed post-neutron mass A_{post}. Experimental data [49] (full points) are compared with the result of the GEF code [11] (open points).*

Simulation
The simulation of the nuclear-charge distributions for fixed post-neutron mass starts from the calculated pre-neutron nuclide distribution and the excitation energy of each individual fragment. The emission of prompt neutrons must be considered, which is constrained by measured mass-dependent prompt-neutron multiplicity distributions. The good agreement with post-neutron fragment distributions shown in figure 8 was obtained by minimizing the potential energy of the scission configuration, approximated by quadrupole-deformed fragments with a tip distance of 3 fm

with respect to their N/Z ratios. However, for the asymmetric fission channels, the value of $<Z>-Z_{UCD}$ had to be increased (decreased) by 0.3 units in the light (heavy) fragment. The mean deformation of the fragments at scission is linked to the mean prompt-neutron multiplicity, considering the amount of intrinsic excitation energy at scission, which is consistent with the description of the even-odd effect in the Z distributions.
The isobaric distributions for $A > 104$ with rather small widths σ_Z, which deviate appreciably from the GEF results, were incompletely measured and completed by estimation [49].

Fragment kinetic energies

The fragment kinetic energy is a key quantity for the energetics of the fission process. With the knowledge of the nuclide distribution of the primary fragments it defines the amount of excitation energy of the fragments, which feeds the emission of prompt neutrons. The pre-scission kinetic energy competes with the intrinsic excitation energy at scission and is thus linked with the even-odd effect in fission-fragment yields, see discussion below.
In the GEF code, the total kinetic energy of the fission fragments is given by subtracting the total excitation energy of the separated fragments from the sum of the initial excitation energy of the fissioning nucleus and the Q value of the fission process. Best agreement with all observables was obtained by assuming that 30% of the energy release from saddle to scission [50] is dissipated into intrinsic excitations. The resulting distribution for $^{235}U(n_{th},f)$ is shown in figure 9. The overall behaviour is in agreement with expectations from systematics. In the model, the shape of the energy distribution for a fixed mass is mainly defined by the distribution of fragment deformations at scission, which is taken as a Gaussian distribution with a maximum in the respective potential minimum and a standard deviation of $\sigma_\beta=0.165$. These shapes define the amount of deformation energy of the separated fragments with respect to their respective ground state, which finally adds up to their intrinsic excitation energy. The kinetic energies obtained with this approach are rather realistic. Also the experimentally observed steeper slope on the high-energy side is reproduced, although the skewness seems to be slightly larger than found in experiment.

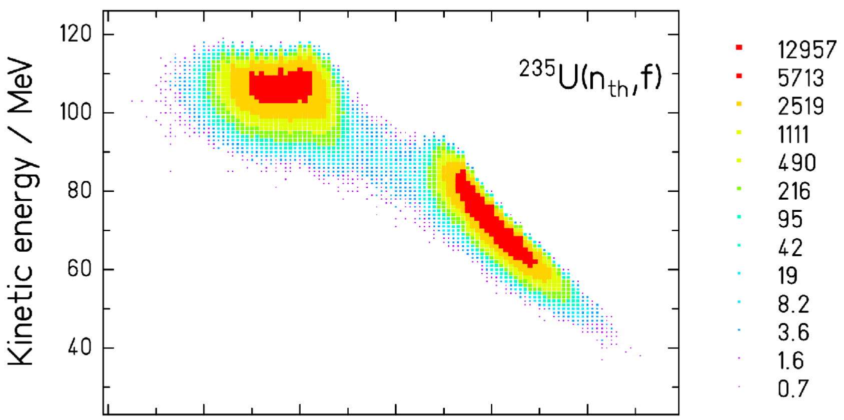

Figure 9. *GEF calculation of the two-dimensional distribution of kinetic energies and fission-fragment masses before emission of prompt neutrons for $^{235}U(n_{th},f)$. The colour scale refers to the number of events of the Monte-Carlo calculation.*

Neutron multiplicities

Besides the mass-dependent mean prompt-neutron yields, see e. g. figure 5, there exist two other experimental results, which have been determined with high accuracy: The mass-integrated neutron-multiplicity distribution and the mean number of prompt fission neutrons.

The measured mean number of prompt-fission neutron yields is compared in table 1 with the values given by the GEF code for some selected systems. The same parameter set was used for all systems. However, the TXE had to be increased by 1.6 MeV, equally shared between the fragments, for odd-*Z* fissioning systems, just as an empirical parameterisation. This is a general effect, found on the average over the whole range of fissioning systems. In contrast, there is no even-odd fluctuation in the neutron number of the fissioning nucleus.

Table 1. *Mean prompt-neutron multiplicities for some selected systems. The measured values are compared with the result of the GEF code.*

System	**E_n**	**Exp.**	**GEF**
^{235}U(n,f)	thermal	2.41 [51]	2.41
^{235}U(n,f)	0.5 MeV	2.46 [52]	2.50
^{235}U(n,f)	5.55 MeV	3.19 [52]	3.29
^{237}Np(n,f)	0.8 MeV	2.73 [35]	2.79
^{237}Np(n,f)	5.55 MeV	3.46 [35]	3.54
^{239}Pu(n,f)	thermal	2.88 [51]	3.02
^{252}Cf(sf)	---	3.77 [53]	3.73

Figure 10 demonstrates the good agreement of the calculated neutron-multiplicity distributions for ^{235}U(n_{th},f), ^{239}Pu(n_{th},f) and ^{252}Cf(sf) with the experimental data [51, 54] compiled in ref. [55]. Like in the case of the fragment kinetic energies, the width is assumed to be mostly caused by the distribution of fragment deformations at scission.

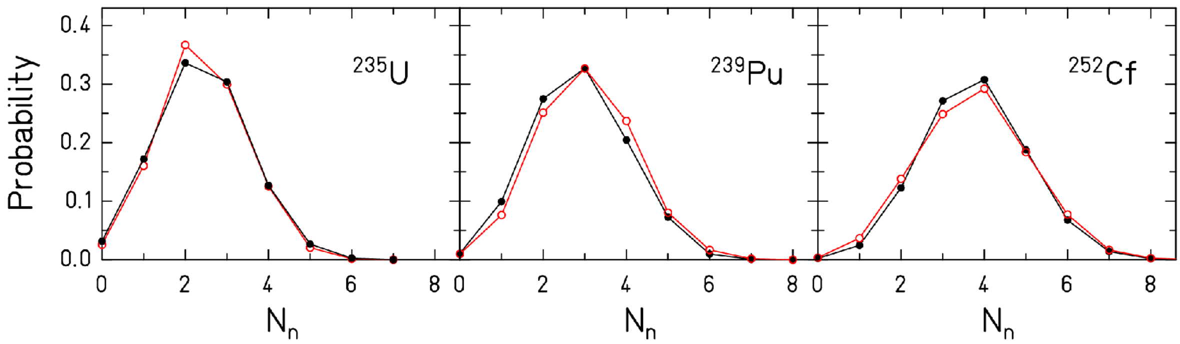

Figure 10. *Measured prompt-neutron multiplicity distributions [51, 54] (full symbols) for ^{235}U(n_{th},f) (left part), ^{239}Pu(n_{th},f) (middle part) and ^{252}Cf(sf) (right part) are compared to the results of the GEF code (open symbols).*

Prompt-neutron spectrum

The experimental prompt-fission-neutron spectra for the systems ^{235}U(n_{th},f) [56] and ^{252}Cf(sf) [57] are compared with results of the GEF code in figure 11. In order to better visualize the deviations, the comparison is shown in linear and logarithmic scale. The lowest panels show a reduced presentation with all spectra normalized to a Maxwellian distribution with the parameter T = 1.32 MeV.
In this calculation, the de-excitation of the separated fragments has been obtained within the statistical model. It is assumed that both the emission of neutrons and the emission of E1 gammas does not change the angular momentum on the average, which seems to be a good approximation in the relevant angular-momentum range [58]. When the yrast line is reached, the angular momentum is carried away by a cascade of E2 gammas. Inverse total neutron cross sections with the optical-

model parameters of ref. [59] were used. Gamma competition at energies above the neutron separation energy was considered. The gamma strength of the giant dipole resonance (GDR) following the description proposed in ref. [60] was applied. The nuclear level density was modelled by the constant-temperature description of v. Egidy and Bucurescu [61] at low energies. A good reproduction of the prompt-neutron spectrum suggests a slight reduction of the temperature values by 15%. The level density was smoothly joined at higher energies with the modified Fermi-gas description of Ignatyuk et al. [62, 63] for the nuclear-state density:

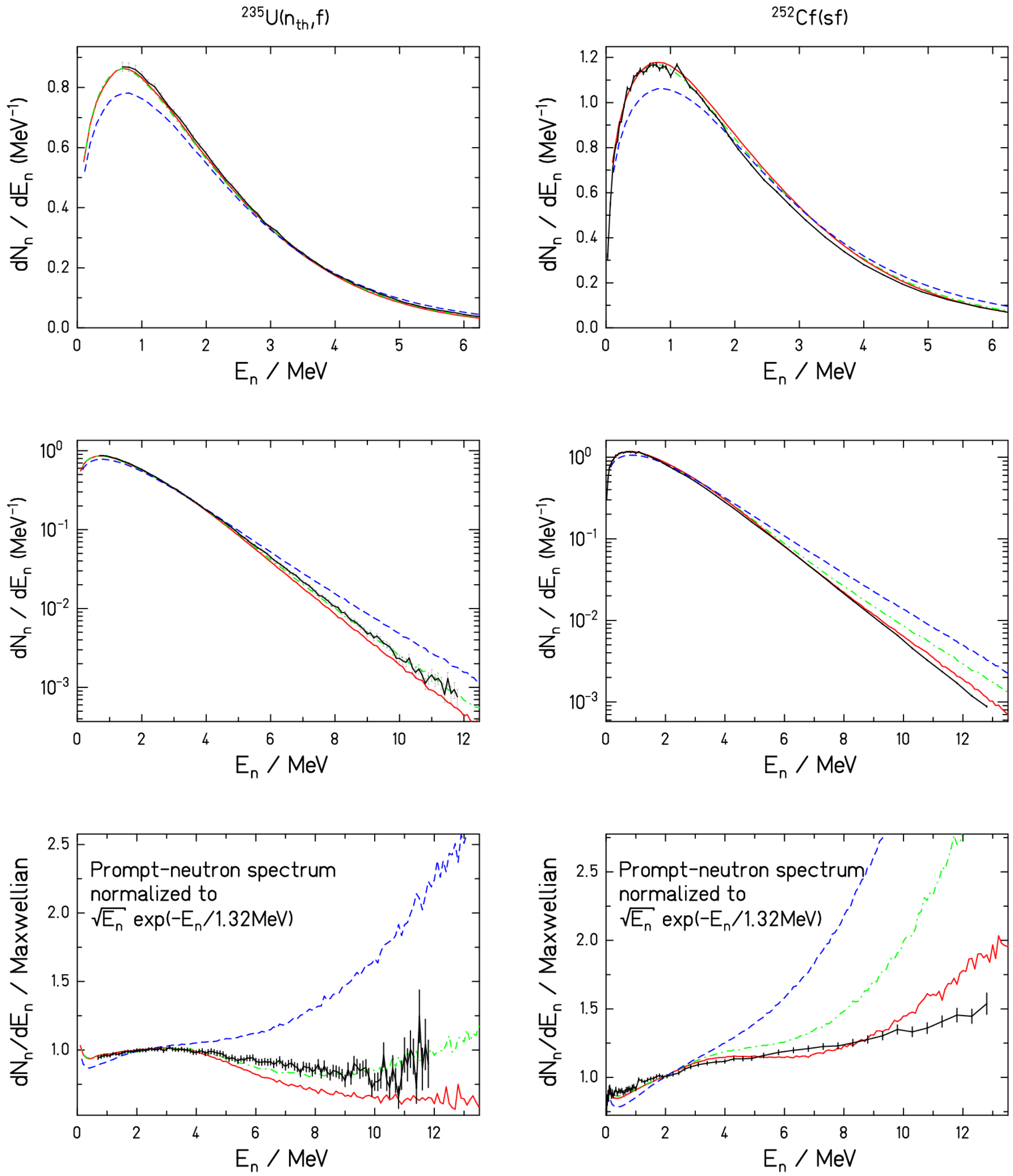

Figure 11. *Experimental prompt-fission-neutron spectra (black lines and error bars) for* $^{235}U(n_{th},f)$ *[56] (left panels) and* $^{252}Cf(sf)$ *[57] (right panels) in comparison with the result of the GEF code in linear and logarithmic scale. In addition to the full calculation (red lines), calculations with constant inverse cross sections (dashed blue lines) and assuming emission from fully accelerated fragments only (green dot-dashed lines) are shown. In the lowest panels, all spectra have been normalized to a Maxwellian with T = 1.32 MeV.*

$$\omega \propto \frac{\sqrt{\pi}}{12\,\tilde{a}^{1/4} U^{5/4}} \exp(2\sqrt{\tilde{a}\,U})$$

with $U = E + E_{cond} + \delta U (1 - \exp(-\gamma E))$, $\gamma = 0.055$ and the asymptotic level-density parameter $\tilde{a} = 0.078 A + 0.115 A^{2/3}$. The shift parameter E_{cond} represents the pairing-condensation energy given by $E_{cond} = -2\,MeV - n\,\Delta_0$, $\Delta_0 = \frac{12}{\sqrt{A}}$ with n = 0,1,2 for odd-odd, odd-A and even-even nuclei, respectively. δU is the ground-state shell correction. A constant spin-cutoff parameter was used. The matching energy is determined from the matching condition (continuous level-density values and derivatives of the constant-temperature and the Fermi-gas part). Values slightly below 10 MeV are obtained. The matching condition also determines a scaling factor for the Fermi-gas part. It is related with the collective enhancement of the level density. A better agreement with the measured prompt-neutron spectrum for the reaction ^{235}U(n_{th},f) was achieved by decreasing the asymptotic level-density parameter $\tilde{a}$ by 14%. The corresponding results are shown by the red full lines. The transformation of the neutron-energies into the laboratory frame was performed considering the acceleration phase [64, 65] after scission by a numerical trajectory calculation.

The rather good reproduction of the measured neutron spectra, especially in the whole lower-energy part, does not give indication for neutron emission at scission [66 ,67 ,68 ,69] although it is difficult to draw a definite conclusion due to the uncertainties in the level densities and in the optical-model parameters.

Simplified calculations show the importance of the optical-model transmission coefficients and of the emission during the acceleration phase. The latter effect is stronger for the system ^{252}Cf(sf), since higher excitation energies and, thus, shorter emission times are involved in this system. Neutron emission during fragment acceleration reduces especially the laboratory energies of the first neutrons emitted at short times from the most highly excited fragments in ^{252}Cf(sf) and allows for a decently consistent description of the two systems with the GEF code, using the same parameter set.

Experimental prompt-fission neutron spectra of the systems ^{239}Pu(n_{th},f) and ^{240}Pu(sf) are compared with the result of the GEF code in figures 12 and 13, again using the same model parameters. Obviously, the data are very well reproduced.

In general, the GEF code reproduces the available experimental fission-prompt-neutron spectra rather well. This qualifies the GEF code for estimating prompt-neutron spectra in cases where experimental data do not exist. It also seems to be a suitable tool for improving evaluations.

Prompt-gamma emission

In figure 14, the calculated prompt-gamma spectrum for the system ^{235}U(n_{th},f) is compared with the experimental data of ref. [79]. One can distinguish the signatures of the different contributions to the gamma strength. The E1 emission from the GDR dominates the high-energy part above 2 MeV. E2 emission from rotational bands at the yrast line strongly fills up the spectrum below 2 MeV. The amount of E2 emission is constrained by the angular-momentum distribution of the fission fragments [70].

Detailed experiments with very high counting statistics and high-granularity detectors, e.g. with the Darmstadt-Heidelberg Crystal ball, have been performed for spontaneous fission of ^{252}Cf. These experiments cover an energy range up to 80 MeV including the whole GDR and extending to the postulated radiation from nucleus-nucleus coherent bremsstrahlung of the accelerating fission fragments [71], which is not considered in the GEF code. Several theoretical studies of the many complex features of these data have been performed, mostly with modified versions of the CASCADE code [72], see e.g. refs. [73, 74]. Figure 15 shows an overview on these data in comparison with the result of the GEF code up to 15 MeV. Obviously, the complex features of this spectrum are fairly well reproduced, in particular the kink near 8 MeV, approaching the peak energy of the GDR. The variation of the spectrum shape for different mass gates, which is at least qualitatively reproduced by the GEF code, has been understood by the influence of shell effects, especially for nuclei near ^{132}Sn, on the de-excitation process [75].

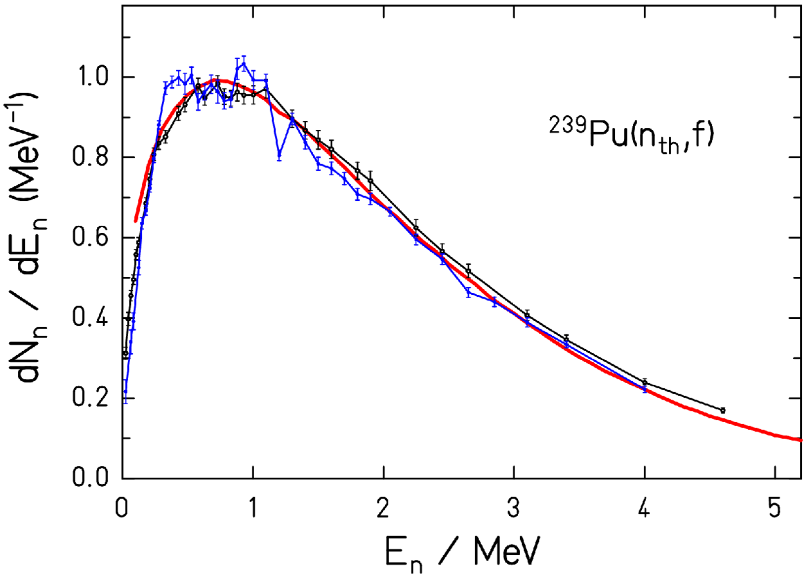

Figure 12. *Experimental prompt-fission-neutron spectrum for the system ^{239}Pu(n_{th},f) from ref. [76] (black open symbols) and from ref. [77] (blue full symbols) in comparison with the result of the GEF code (red thick full line). The calculated spectrum was normalized to the measured total neutron multiplicity ($\bar{\nu}$=2.88 [51]) by a factor of 0.954. The measured spectra are slightly scaled for minimizing the overall deviations from the calculated spectrum in order to better compare the spectral shapes.*

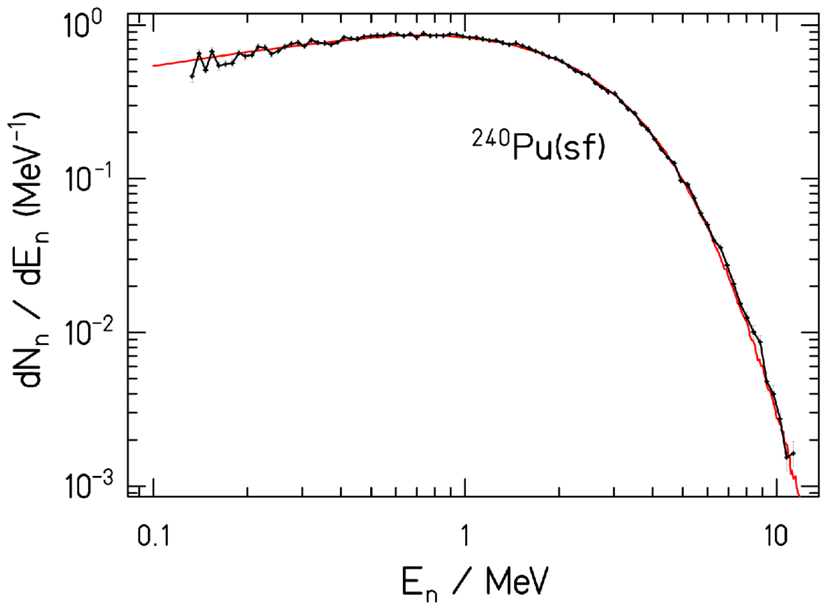

Figure 13. *Experimental prompt-fission-neutron spectrum for the system ^{240}Pu(sf) from ref. [78] (black symbols) in comparison with the result of the GEF code (red line). The measured data were scaled to the height of the calculated spectrum. Since the experiment covers especially well the lower-energy range, a double-logarithmic presentation was chosen.*

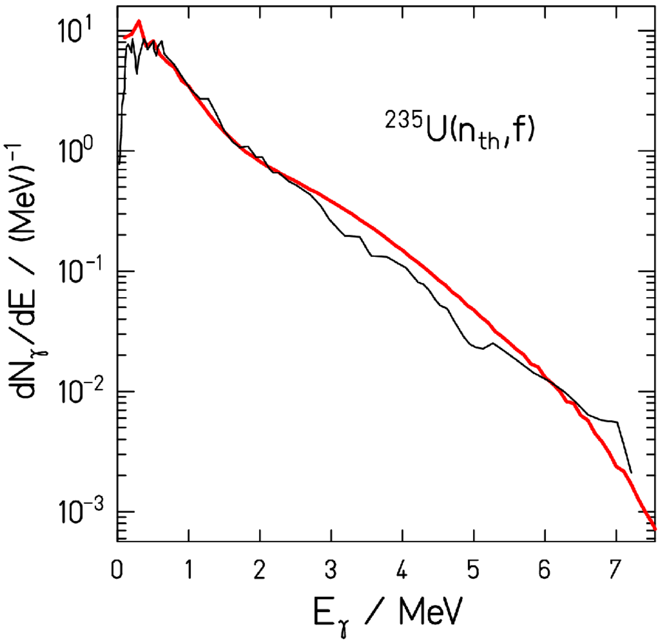

Figure 14. *Experimental prompt-gamma spectrum for $^{235}U(n_{th},f)$ [79] (thin black line) in comparison with the result of the GEF code (thick red line).*

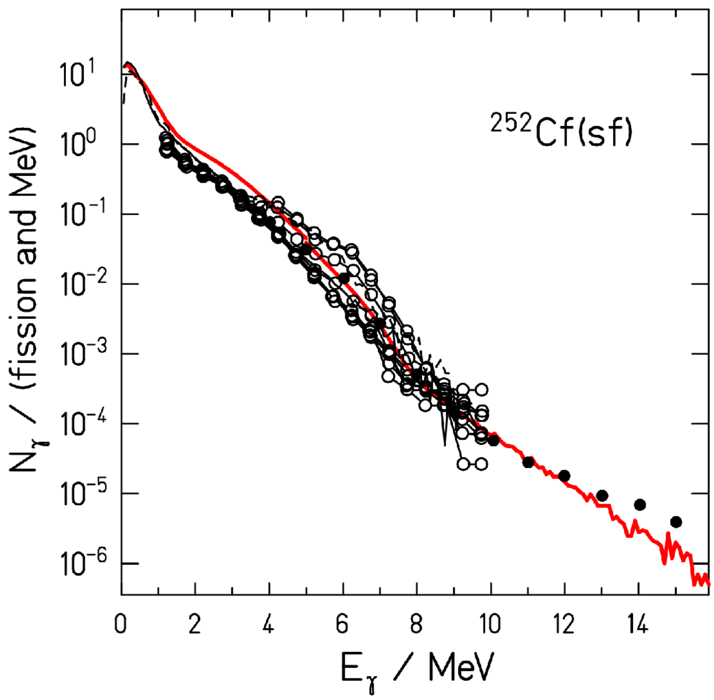

Figure 15. *Experimental prompt-gamma spectrum for $^{252}Cf(sf)$ (data points and thin solid and dashed black lines) in comparison with the result of the GEF code (thick red line). Thin solid line: Raw spectrum from ref. [80], gate on the mass of the heavy fragment $126 \leq A_H \leq 136$. Thin dashed line: Raw spectrum from ref [80], gate on $144 \leq A_H \leq 154$. Open symbols: Deconvoluted spectra from ref. [81] with gates on different mass regions. Full symbols: Raw data from ref. [82].*

Conclusion

The semi-empirical fission model, implemented in the GEF code, reproduces a large variety of observables with a good precision in a consistent way without further adjustment to specific fissioning systems with a unique parameter set. With this global approach one is able to predict several characteristic quantities of the fission process, e.g. the energy and multiplicity distribution of prompt-fission neutrons and prompt-fission gammas without the need for specific experimental information for the respective system, e.g. measured mass-TKE distributions. All properties of the fission fragments that are considered in the code (e.g. nuclear charge, mass, excitation energy, angular momentum) are sampled in the corresponding multi-dimensional parameter space by a Monte-Carlo technique. Thus, all respective correlations are preserved. Moreover, GEF is an event generator where correlations between all observables considered in the code are provided on an event-by-event basis.

Part of this work has been supported by the NEA of the OECD (http://www.oecd-nea.org/), by the EFNUDAT (http://www.efnudat.eu/) and by the ERINDA (http://www.erinda.org/) projects of EURATOM.

1 A. C. Wahl, Report LA-13928 (2002), Los Alamos National Laboratory.
2 D. Seeliger et al., Report INDC(GDR)-057 (1990), IAEA Vienna.
3 D. G. Madland, Report LA-UR-98-797 (1998), Los Alamos National Laboratory.
4 I.-E. Visan, A. Tudora, J. Nucl. Res. Development 1 (2011) 43.
5 K.-H. Schmidt et al., Nucl. Phys. A 665 (2000) 221.
6 M. G. Itkis et al., Sov. J. Nucl. Phys. 52 (1990) 601.
7 A. N. Andreyev et al., Phys. Rev. Lett. 105 (2010) 252502.
8 S. I. Mulgin, K.-H. Schmidt, A. Grewe, S. V. Zhdanov, Nucl. Phys. A 640 (1998) 375.
9 J. P. Unik et al., Proc. Symp. Phys. Chem. Fission, Rochester 1973, IAEA Vienna (1974), vol. 2, p. 19.
10 B. D. Wilkins, E. P. Steinberg, R. R. Chasman, Phys. Rev. C 14 (1976) 1832.
11 http://www.cenbg.in2p3.fr/GEF, http://www.khs-erzhausen.de
12 I. Ragnarsson, R. K. Sheline, Phys. Scr. 29 (1984) 385.
13 M. Brack et al., Rev. Mod. Phys. 44 (1972) 320.
14 U. Mosel, H. Schmitt, Phys. Rev. C 4 (1971) 2185.
15 K.-H. Schmidt, A. Kelic, M. V. Ricciardi, Europh. Lett. 83 (2008) 32001.
16 J. R. Nix, Ann. Phys. 41 (1967) 52.
17 A. V. Karpov, P. N. Nadtochy, D. V. Vanin, G. D. Adeev, Phys. Rev. C 63 (2001) 054610.
18 A. V. Karpov, G. D. Adeev, Eur. Phys. J. A 14 (2002) 169.
19 H. Nifenecker, J. Physique Lett. 41 (1980) 47.
20 B. Bouzid et al., J. Phys. G: Nucl. Part. Phys. 24 (1998) 1029.
21 D. Bucurescu, T. von Egidy, Phys. Rev. C 72 (2005) 06730.
22 L. Bonneau, P. Quentin, I. N. Mikhailov, Phys. Rev. C 75 (2007) 064313.
23 F. Gönnenwein, I. Tsekhanovich, V. Rubchenya, Intern. J. Mod. Phys. E 16 (2007) 410.
24 S. G. Kadmensky, Phys. Atom. Nuclei 71 (2008) 1193.
25 H. Naik, S. P. Dange, R. J. Singh, A. V. R. Reddy , Eur. Phys. J. A 31 (2007) 195.
26 L. G. Moretto, G. F. Peaslee, G. J. Wozniak, Nucl. Phys. A 502 (1989) 453c.
27 H. Goutte, J. F. Berger, P. Casoli, D. Gogny, Phys. Rev. C 71 (2005) 024316.
28 J. Randrup, P. Möller, A. J. Sierk, Phys. Rev. C 84 (2011) 034613.
29 A. S. Jensen, T. Døssing , Proc. Symp. Phys. Chem. Fission, Rochester 1973, IAEA Vienna (1974), vol. 1, p. 40.
30 A. V. Voinov et al., Phys. Rev. C 79 (2009) 031301.
31 V. M. Kolomietz, S. Åberg, S. V. Radionov, Phys. Rev. C 77 (2008) 014305.
32 W. J. Swiatecki, S. Bjørnholm, Phys. Rep. 4 (1972) 32.
33 U. Brosa, S. Grossmann, A. Müller, Phys. Rep. 197 (1990) 167.
34 N. Dubray, H. Goutte, J.-P. Delaroche, Phys. Rev. C 77 (2008) 014310.
35 A. A. Naqvi, F. Käppeler, F. Dickmann, R. Müller, Phys. Rev. C 34 (1986) 21.
36 C. Budtz-Jørgensen, H.-H. Knitter, Nucl. Phys. A 490 (1988) 307.
37 A. C. Wahl, At. Data Nucl. Data Tables 39 (1988) 1.
38 A. V. Voinov et al., Phys. Rev. C 79 (2009) 031301.
39 M. Guttormsen et al., Phys. Rev. C 68 (2003) 034311.
40 Y. Alhassid, G. F. Bertsch, L. Fang, Phys. Rev. C 68 (2003) 044322.
41 K.-H. Schmidt, B. Jurado, Phys. Rev. Lett. 104 (2010) 21250.
42 K.-H. Schmidt, B. Jurado, Phys. Rev. C 82 (2011) 014607.
43 K.-H. Schmidt, B. Jurado, Phys. Rev. C 83 (2011) 061601.
44 G. G. Dussel, S. Pittel, J. Dukelsky, P. Sarriguren , Phys. Rev. C 76 (2007) 011302.
45 R. Capote et al., Nucl. Data Sheets 110 (2009) 3107.
46 M. Caamaño, F. Rejmund, K.-H. Schmidt, J. Phys. G: Nucl. Part. Phys. 38 (2011) 035101.
47 S. Steinhäuser et al., Nucl. Phys. A 634 (1998) 89.
48 K.-H. Schmidt, B. Jurado, arXiv:1007.0741v1[nucl-th] (2010).
49 W. Lang et al., Nucl. Phys. A 345 (1980) 34.
50 M. Asghar, R. W. Hasse, J. Phys. Colloques 45 (1984) C6-455.
51 M. S. Zucker, N. E. Holden, Report BNL-38491 (1986).
52 R. Müller, A. A. Naqvi, F. Käppeler, F. Dickmann, Phys. Rev. C 29 (1984) 885.
53 E. J. Axton, Nucl. Stand. Ref. Data (1985) 214.
54 R.R. Spencer, R. Gwin, R.W. Ingle, Nucl. Science Engin. 80 (1982). 603 .
55 J. M. Verbeke et al., Report UCRL-AR-228518, Lawrence Livermore Laboratory (2010).
56 N. V. Kornilov et al., Nucl. Science Engin. 165 (2010) 117.
57 W. Mannhart, INDC(NDS)-220/L (1989) 305, IAEA, Vienna.
58 J. R. Huizenga, R. Vandenbosch, Phys. Rev. 120 (1960) 130.
59 A. J. Koning, J. P. Delaroche, Nucl. Phys. A 713 (2003) 231.
60 A. R. Junghans et al., Phys. Lett. B 670 (2008) 200.
61 T. von Egidy, D. Bucurescu, Phys. Rev. C 78 (2008) 05130.
62 A. V. Ignatyuk, G. N. Smirenkin, A. S. Tishin, Sov. J. Nucl. Phys. 21 (1975) 255.
63 A. V. Ignatyuk, Hadrons Nuclei Appl. 3 (2001) 287.

64 V. P. Eismont, Atomn. Ener. 19 (1965) 113.
65 V. M. Maslov et al., Eur. Phys. J. A 18 (2003) 93.
66 N. V. Kornilov et al., Nucl. Phys. A 686 (2001) 187.
67 G. V. Danilyan et al., Phys. Atom. Nucl. 71 (2008) 200.
68 G. A. Petrov et al., Phys. Atom. Nucl. 71 (2008) 1137.
69 N. Carjan. M. Rizea, Phys. Rev. C 82 (2010) 01461.
70 H. Naik, S. P. Dange, R. J. Singh, Phys. Rev. C 71 (2005) 014304.
71 S. P. Maydanyuk et al., Phys. Rev. C 82 (2010) 014602.
72 F. Pühlhofer, Nucl. Phys. 280 (1977) 267.
73 D. J. Hofman et al., Phys. Rev. C 47 (1993) 1103.
74 H. van der Ploeg et al., Nucl. Phys. A 569 (1994) 83.
75 H. von der Ploeg et al., Phys. Rev. C 52 (1995) 1915.
76 A. A.Bojcov et al., 6th All Union Conf. Kiev (1983) Vol. 2, p. 294.
77 A. Lajtai et al., Nucl. Data Conf., Santa Fe (1985) Vol. 1, p. 613.
78 L. V. Drapchinsky et al., communicated by N. Capote, 2012.
79 R. W. Pelle, F. C. Maienschein, Phys. Rev. C 3 (1971) 373.
80 P. Singer et al., Z. Phys. A 359 (1997) 41.
81 A. Hotzel et al., Z. Phys. A 356 (1996) 299.
82 D. Pandit et al., Phys. Lett. B 690 (2010) 473.

APPENDIX 1

This appendix gives a short summary of the main GEF-model details and parameter values, if not yet specified in the main text. More details can be found in the source code [1].

The shape of the nascent fragments at scission is considered to be defined by proton shell effects. This is consistent with the apparent dominant role of protons to define the size of the heavy fragment in asymmetric fission. According to global features of shell-model calculations [2] (inclined valleys in the particle-number – deformation plane formed by shell effects) and adjusted to the prompt-neutron yields, the deformation of the nascent fragments in the light and the heavy groups of the asymmetric fission channels are given by:

$$\beta_{light} = 0.04 \cdot (Z_{light} - 26.6) \quad , \quad \beta_{heavy} = 0.035 \cdot (Z_{heavy} - 48) \quad .$$

Deviating from this behaviour, the nascent heavy fragment of the standard 1 fission channel is assumed to be spherical. The deformations β_{light} and β_{heavy} of the nascent fragments of the super-long fission channel that appears predominantly at higher excitation energies are determined by minimizing the potential energy of the scission configuration of two nuclei at a tip distance of 3 fm.

The deformation energy of the nascent fragments, which is part of the excitation energy of the separated fragments, is dominated by the macroscopic contribution. Therefore, and since the shell effects at the large deformations encountered at scission are uncertain, the contribution of shell effects to the deformation energy is neglected.

The charge polarization at scission (related to the deviation of the *N*/*Z* ratios of the fragments from the value of the fissioning nucleus) is calculated by minimizing the potential energy of the same scission configuration for a given mass division. In order to obtain agreement with experimental data, the mean number of protons in the light (heavy) fragment for a fixed mass is reduced (increased) by 0.3 units, except for the super-long fission channel.

The mean positions of the shells in proton number in the heavy fragment , which are responsible for the fission channels, are given by the following empirical relations [3]:

$$\bar{Z}_{S1} = 51.5 + 23.3 \cdot \left(\frac{Z_{CN}^{1.3}}{A_{CN}} - 1.5 \right)$$ (The deviation from Z=50 may be caused by the neck.)

$$\bar{Z}_{S2} = 54.05 + 21.7 \cdot \left(\frac{Z_{CN}^{1.3}}{A_{CN}} - 1.5 \right)$$

$$\bar{Z}_{S3} = 58.55 + 21.7 \cdot \left(\frac{Z_{CN}^{1.3}}{A_{CN}} - 1.5 \right)$$

The exact positions of the fission channels are determined by maximizing the level density in the mass-asymmetry degree of freedom, considering the macroscopic potential in mass-asymmetry and the shell effects.

The relevant macroscopic potential in the mass-asymmetry degree of freedom [4] is given by:

$$U_{asym} / \mathrm{MeV} = \left(A_f - \frac{A_{CN}}{2} \right)^2 \cdot \frac{8}{A_{CN}^2} \cdot \exp\left(-9.05 + 4.85 \cdot \ln\left(\frac{Z_{CN}^2}{2.3 \cdot A_{CN}} \right) \right)$$

The width of the super-long fission channel in mass is given by the systematics of ref. [5].

Macroscopic fission barriers from ref. [6] and macroscopic nuclear masses from ref. [7], including the congruence energy, are used.

Ground-state shell corrections are taken from ref. [8].

The potential-energy difference from saddle to scission from ref. [9] is parameterised by :

$$\Delta E_{pot}/\mathrm{MeV}=0.08\cdot\left(\frac{Z_{CN}^2}{A^{1/3}}-1270\right)+11 \quad .$$

A fraction of 30% of this energy is assumed to be dissipated into intrinsic excitation energy on the way to scission. Together with the initial excitation energy of the fissioning nucleus above the respective fission saddle, this energy is subject to energy sorting before scission.

The relative yield and the width of a specific fission channel is determined by the level density above the respective effective saddle. The effective saddle is taken at the point in collective coordinate space where the level density in fission direction is minimum and the level density in mass asymmetry is maximum at the specific intrinsic excitation energy of the system above the saddle. The height of the respective saddle point is empirically determined by the measured yields of all available fissioning systems with the help of the separability principle. The zero-point motion in the different normal modes is considered in an empirical way.

The strengths of the shells behind the fission channels are approximated by quadratic functions, resulting in Gaussian Z distributions in the constant-temperature approximation:

$$\delta U_{S1}/\mathrm{MeV}=-5.8+0.75\cdot(Z_f-\bar{Z}_{S1})^2\cdot\left|1-0.055\cdot(82-N_{CN}\cdot 50/Z_{CN})\right|$$

$$\delta U_{S2}/\mathrm{MeV}=-4.0+0.5\cdot(Z_f-\bar{Z}_{s2})^2$$

$$\delta U_{S3}/\mathrm{MeV}=-5.8\cdot(1-0.005\cdot(Z_{CN}-\bar{Z}_{S3}-37)^2)+0.22\cdot(Z_f-\bar{Z}_{S3})^2$$

In addition to the proton shell, an additional contribution to δU_{S1} by the N=82 shell is assumed. The strength of the standard 1 fission channel is enhanced for isotopes of americium and the neighbouring elements by an additional shell effect, assumed to be present in the light fragment around Z=44. This effect is clearly visible in the data.

$$\delta U_{S1-light}/\mathrm{MeV}=-0.8+0.1\cdot(Z_{CN}-Z_f-44.85)^2$$

In addition, there is a specific reduction of the S1 fission channel for systems with very low excitation energies at scission, which is strongly required by the low-energy data of light systems below plutonium. For the standard 2 fission channel, an additional rectangular function with a full width of 14 mass units is convoluted to the resulting Gaussian distribution.

The strength of the standard 3 fission channel depends on the possible superposition of shells in the light and the heavy fragment for a given compound nucleus. This should be considered as a very preliminary parameterisation of the standard 3 fission channel.

Tunneling through the outer fission barrier is taken into account with the Hill-Wheeler expression and a transmission parameter close to $\hbar\omega=2\pi\cdot 0.3\,\mathrm{MeV}$. (Note that the transmission through the inner barrier has no influence on the fission-fragment mass distribution.)

1 http://www.cenbg.in2p3.fr/GEF, http://www.khs-erzhausen.de
2 I. Ragnarsson, R. K. Sheline , Phys. Scr. 29 (1984) 38.
3 C. Böckstiegel et al., Nucl. Phys. A 802 (2008) 12.
4 S. I. Mulgin, K.-H. Schmidt, A. Grewe, S. V. Zhdanov , Nucl. Phys. A 640 (1998) 375.
5 A. Ya. Rusanov, V. V. Pashkevich, M. G. Itkis, Phys. Atomic Nuclei 62 (1999) 547.
6 W. D. Myers, W. J. Swiatecki , Phys. Rev. C 60 (1999) 014606.
7 W. D. Myers, W. J. Swiatecki, Nucl. Phys. A 601 (1996) 14.
8 P. Möller, J. R. Nix, W. D. Myers, W. J. Swiatecki , Atom. Data Nucl. Data Tables 59 (1995) 18.
9 M. Asghar, R. W. Hasse , J. Phys. Colloques 45 (1984) C6-455.

APPENDIX 2

This appendix presents a comprehensive comparison of measured or evaluated fission-fragment mass and nuclear-charge distributions with the results of the GEF code in logarithmic and linear scale. In this way, the quality of the reproduction of the mass yields can be seen over the whole range of fissioning systems. Evaluated data are taken from ENDF VII. All calculations have been performed with a unique set of model parameters.

In figures A2-1 and A2-4 one can observe a good reproduction of the general trends over all spontaneously fissioning systems. Also the transition to the narrow symmetric fission peak between ^{256}Fm and ^{258}Fm, resulting from the superposition of the Standard 1 fission channel in both fragments, is correctly reproduced. When considering the deviations of the GEF calculations from the empirical data, one should take into account that the evaluated data in many cases have only a narrow data basis. Moreover, mass distributions deduced from double-energy measurements under difficult conditions (e.g the data for ^{238,240,242}Pu(sf)) may suffer from an imprecise mass calibration and limited mass resolution. The measurements of the heaviest elements were made with very weak samples and, thus, have low statistics.

In the mass distributions of thermal-neutron-induced fission, shown in figure A2-2 and A2-5, there is again a good reproduction of the over-all trend. The mass and *Z* yields of some systems, which have been investigated experimentally with great care and effort, e.g. ^{233,235}U(n_{th},f), ^{239}Pu(n_{th},f) are almost perfectly reproduced by GEF, including the even-odd effect in the *Z* yields. The evaluation for ^{227}Th(n_{th},f) shows some contribution in the inner wings of the distribution that are not expected from systematics and that are not reproduced by GEF. GEF calculations also deviate appreciably from the evaluated mass distribution for ^{254}Es(n_{th},f) and even more for ^{255}Fm(n_{th},f) (not shown). The central minima of these evaluated mass distributions appear at too high masses and are not compatible with the high neutron yields of these systems from measurements or systematics. It seems that the authors of the evaluation did not properly account for prompt-neutron emission.
The set of experimental data for ^{241}Pu(n_{th},f) seems to suffer from some background. The high yields in the wings of the heavy peak deviate from both the evaluation and the result of the GEF code.
In this situation, it is difficult to attribute the discrepancies between evaluated and calculated mass distributions to some shortcomings of the GEF code.

The mass distributions of all systems investigated with fast neutrons, shown in figure A2-3 and A2-6, are rather well reproduced by the GEF code. Slight deviations, mostly in the wings, appear for a few systems.

In summary, the GEF code gives an overall rather good reproduction of the mass and *Z* yields in the considered range of fissioning systems.

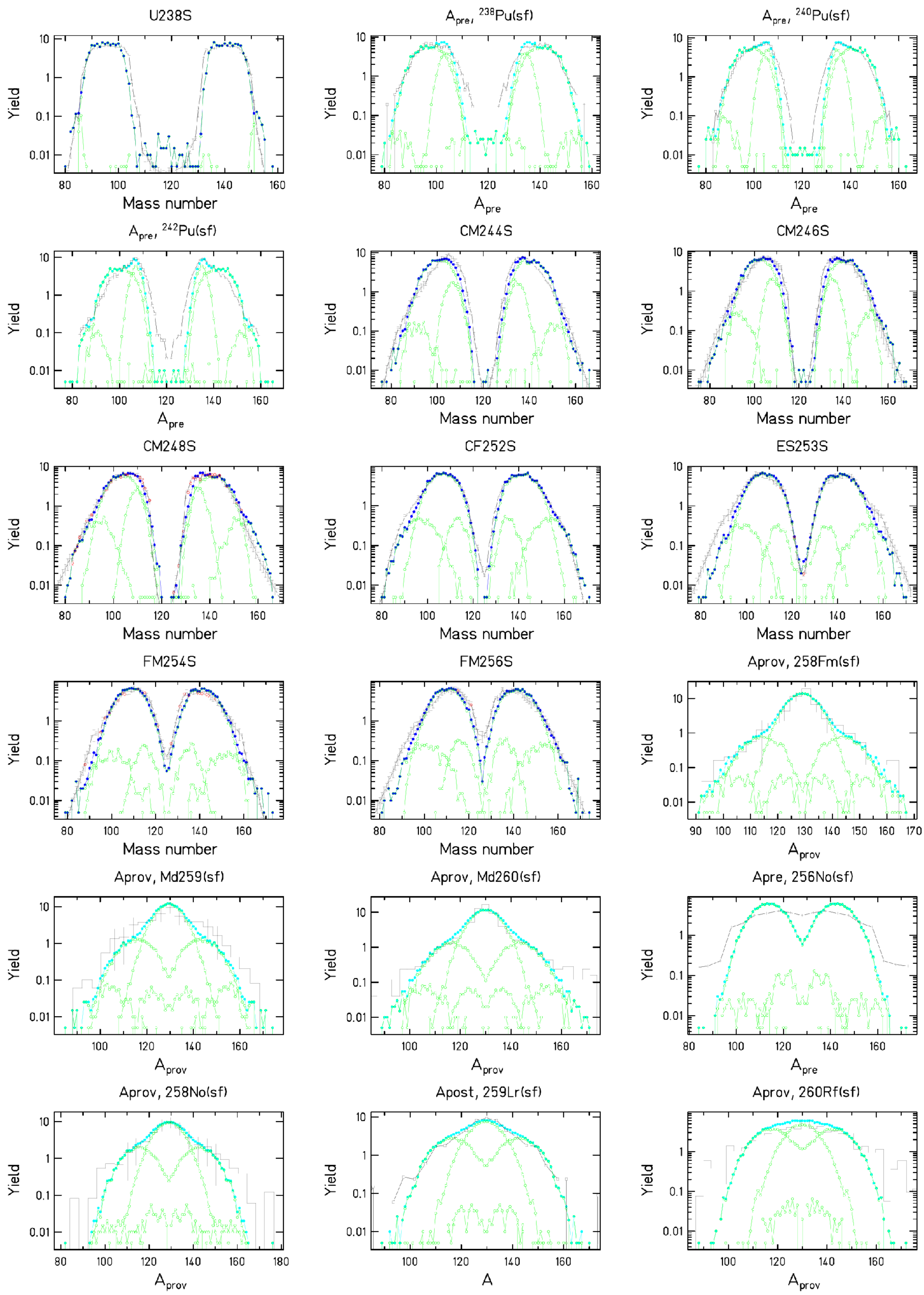

Figure A2-1. *Mass and Z distributions of fission fragments from spontaneous fission. (In most cases the post-neutron masses are shown. A_{prov} is the "provisional mass" that is directly deduced from the ratio of the kinetic energies of the fragments and, thus, it is not corrected for neutron emission.) Measured or evaluated data (black lines, respectively histogram) are compared with predictions of the GEF code [1] (pink and green lines). The contributions of different fission channels are shown. (See [1] for references of the data.) The mass yields marked by red symbols refer to measured data compiled in ref. [2].*

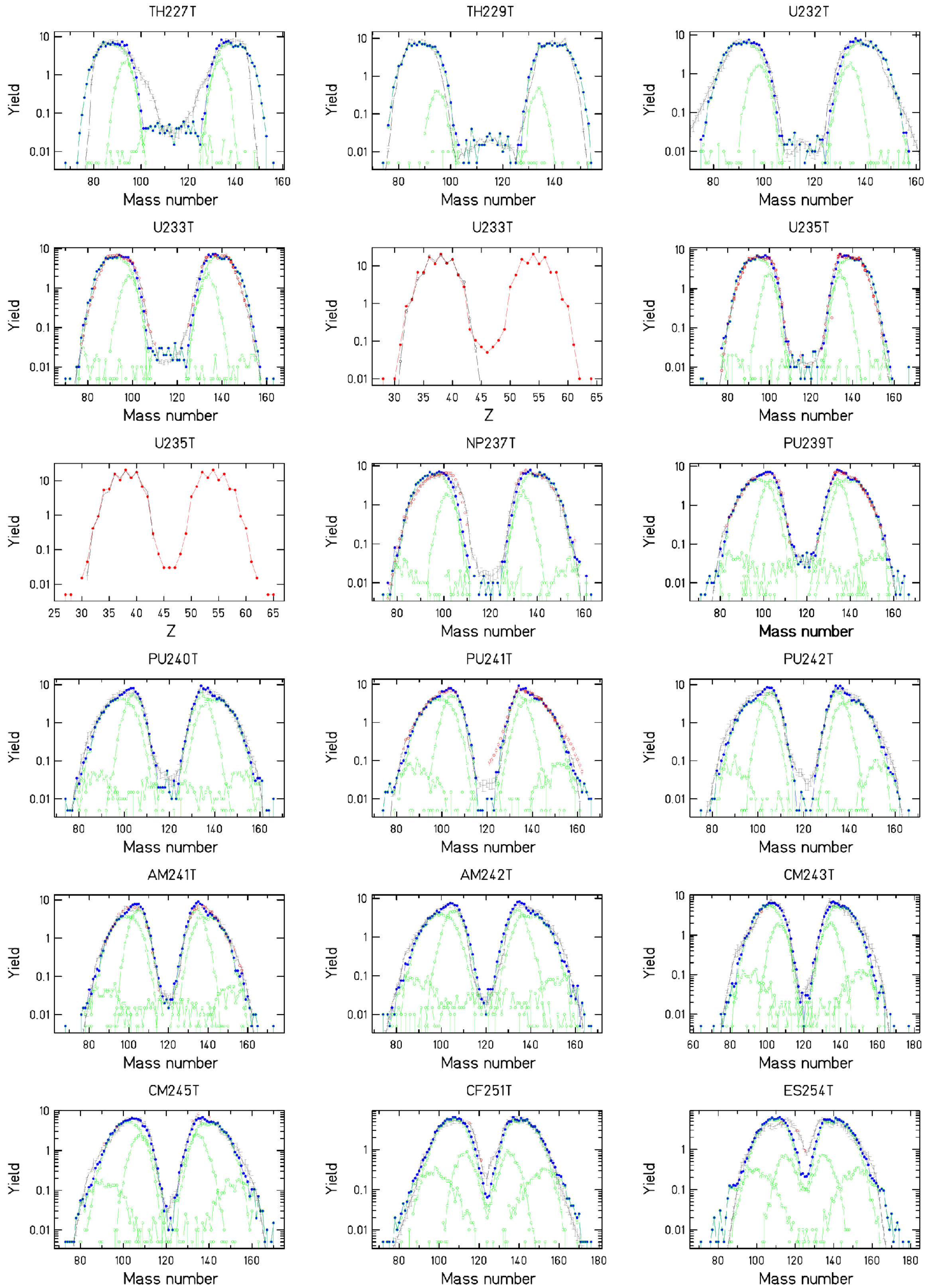

Figure A2-2. *Nuclear-charge and mass distributions of fission fragments from thermal-neutron-induced fission. Measured or evaluated data (black lines, respectively histogram) are compared with predictions of the GEF code [1] (red and green lines). The contributions of different fission channels are shown. (See [1] for references of the data.) The mass yields marked by red symbols refer to measured data compiled in ref. [2].*

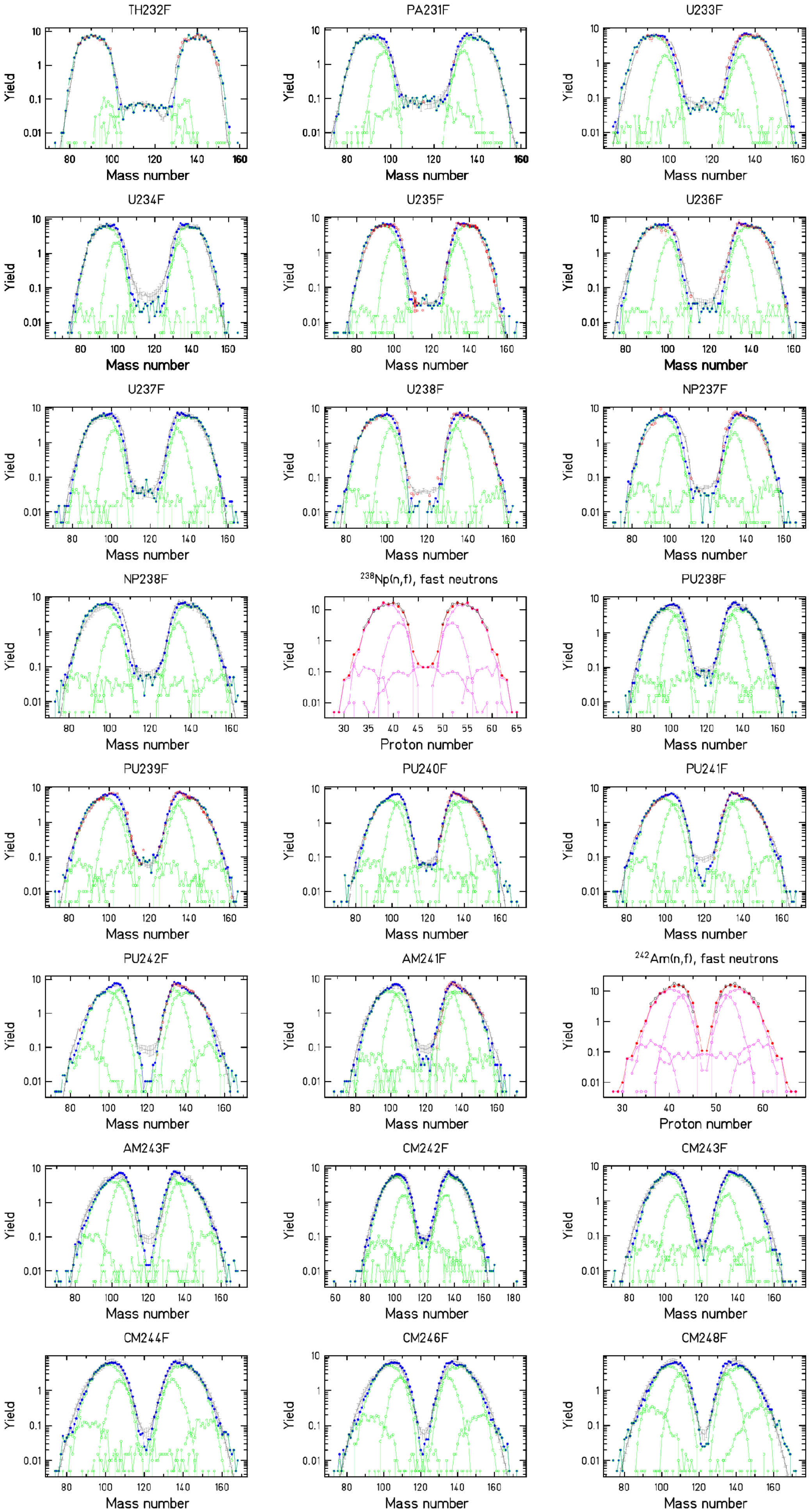

TH232F
PA231F
U233F
U234F
U235F
U236F
U237F
U238F
NP237F
NP238F
^{238}Np(n,f), fast neutrons
PU238F
PU239F
PU240F
PU241F
PU242F
AM241F
^{242}Am(n,f), fast neutrons
AM243F
CM242F
CM243F
CM244F
CM246F
CM248F
Yield
Mass number
Proton number

Figure A2-3. *(On previous page) Nuclear-charge and mass distributions of fission fragments from fast-neutron-induced fission. Measured or evaluated data (black lines, respectively histogram) are compared with predictions of the GEF code [1] (red and green lines). The contributions of different fission channels are shown. (See [1] for references of the data.) The mass yields marked by red symbols refer to measured data compiled in ref. [2].*

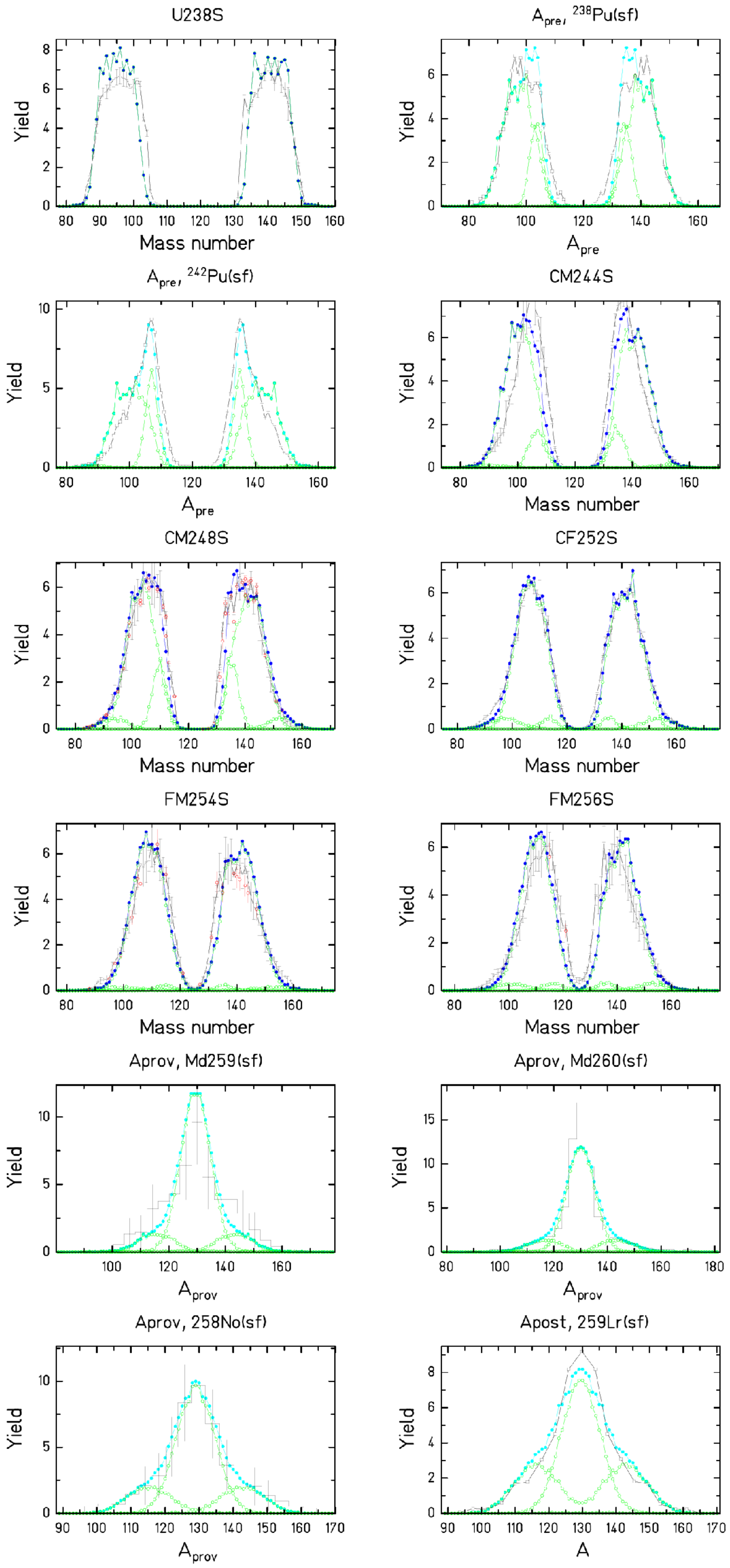

Figure A2-4*. Like figure A2-1, but in linear scale.*

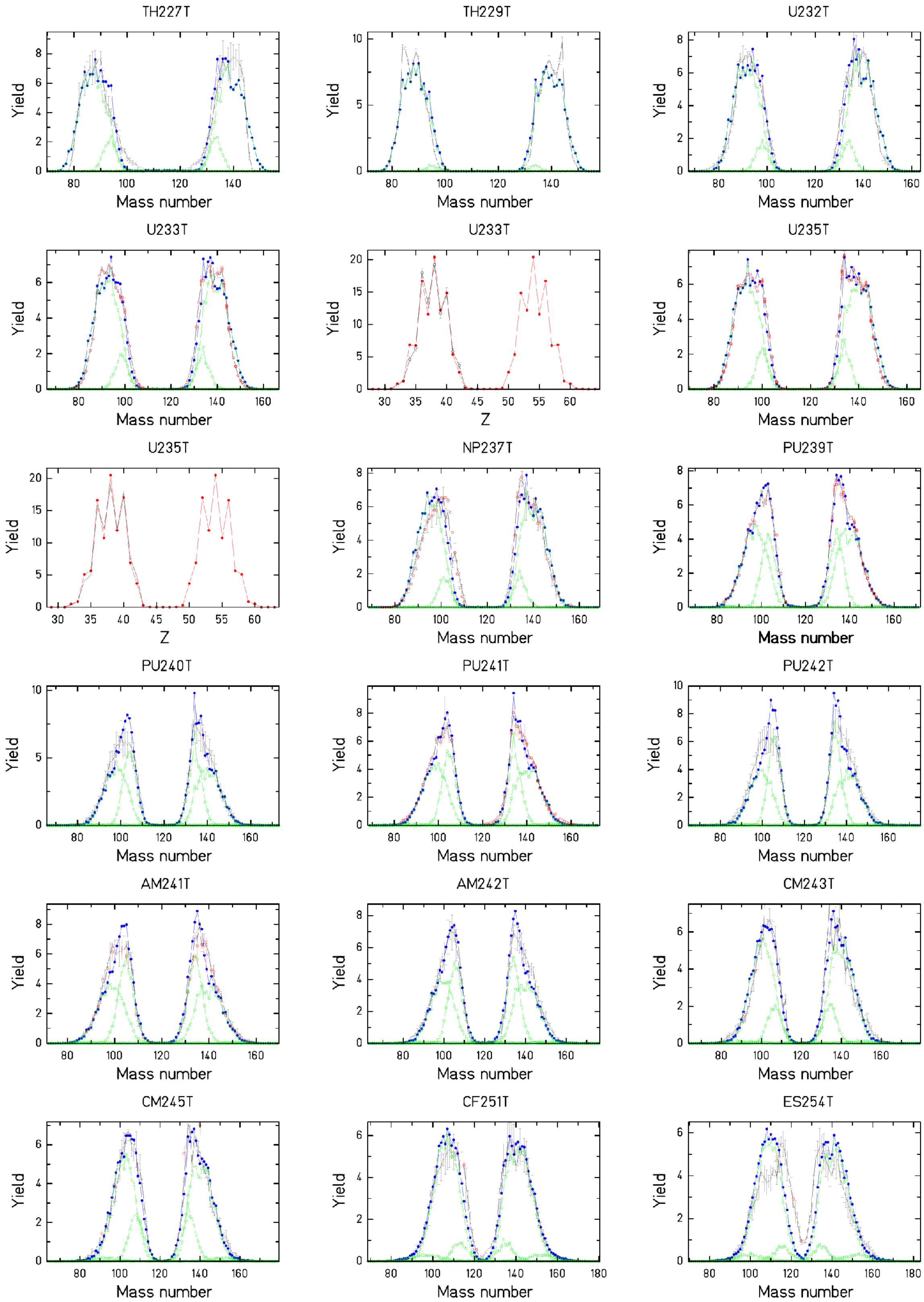

Figure A2-5. *Like figure A2-2, but in linear scale.*

Figure A2-6. *(On next page) Like figure A2-3, but in linear scale.*

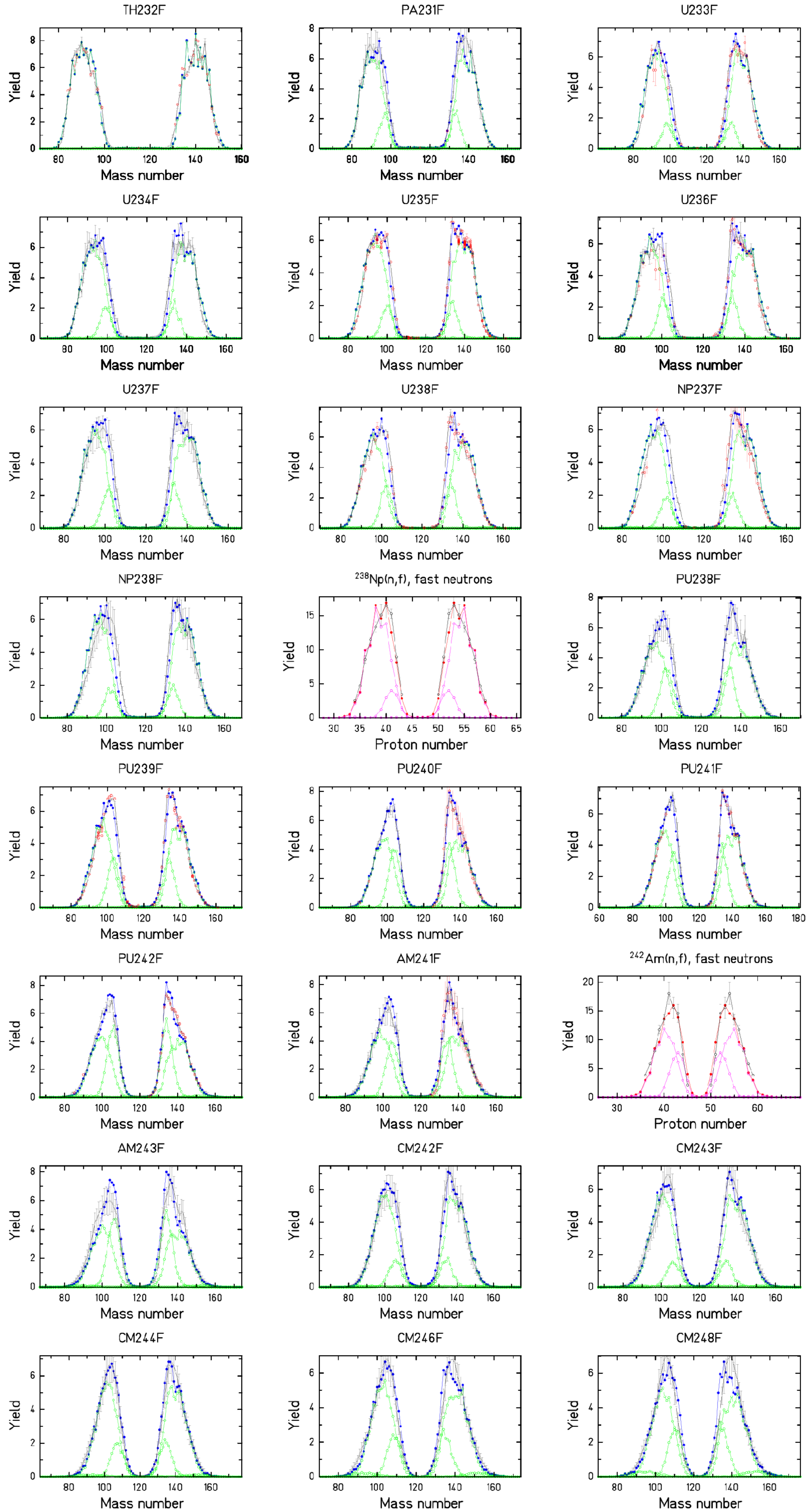
TH232F
PA231F
U233F
U234F
U235F
U236F
U237F
U238F
NP237F
NP238F
238Np(n,f), fast neutrons
PU238F
PU239F
PU240F
PU241F
PU242F
AM241F
242Am(n,f), fast neutrons
AM243F
CM242F
CM243F
CM244F
CM246F
CM248F
Yield
Mass number
Proton number

1 http://www.cenbg.in2p3.fr/GEF, http://www.khs-erzhausen.de
2 R. W. Mills, PhD thesis, University of Birmingham, 1995.